Landslides (2020) 17:1605–1618
DOI 10.1007/s10346-020-01390-x
Received: 19 August 2019
Accepted: 9 March 2020
Published online: 19 March 2020

Zheng-Yi Feng · Hao-Yang Huang · Su-Chin Chen

Analysis of the characteristics of seismic and acoustic signals produced by a dam failure and slope erosion test

Abstract Landslides and floods occur with a significant generation of energy release producing seismic and acoustic signals. The analysis of these signals aims to identify vital and specific characteristics of landslide and flood events, such as frequency content, spectral magnitude, energy variation, and timing of the events. This study examined the seismic and acoustic signals recorded during a large-scale physical dam model failure test. The tests were conducted on the streambed under the No. 2 Bridge in Huisun Forest Experimental Station in Nantou, Taiwan. A dam and a slope model were constructed, and dam failure and slope erosion tests were induced by releasing water to slowly accumulate at the upstream side of the dam and letting water overtop the dam, causing a breach. After dam overtopping, the lowering of the dam crest led to dam failure, causing a large volume of floodwater, resulting in erosion of the toe of the slope model, triggering landslides. Accelerometers and microphones were installed to collect the acoustic and seismic signals produced by the water flow and landslides generated. Unmanned aerial vehicles were used to continuously capture the topography of the slope to produce elevation models to calculate the volumes of the six landslides. Hilbert–Huang transform (HHT) was performed to evaluate the time–frequency spectra for the seismic and acoustic signals, and their spectral magnitudes were discussed. The results showed that the acoustic signals depicted and reacted to the failure event earlier than seismic signals; however, both types of signals were in agreement. The velocity of the flood energy was estimated to be 5.71 and 5.06 m/s by monitoring the seismic signals at different locations of the riverbank and through the analysis of spectral magnitude, respectively. Furthermore, the Arias intensity and the landslide volumes were found to be correlated through a quadratic relationship.

Keywords Seismic signal · Acoustic signal · Dam · Landslide · Time–frequency analysis

Introduction

In mountainous regions, typhoons or intense rainfall often cause large-scale landslides, and a secondary disaster may occur if a considerable amount of debris from the landslide accumulates at the streambed to form a landslide dam. Costa and Schuster (1988) compiled data on landslide dams around the world and identified rainfall, snowmelt, and earthquakes as the main causes of dam-forming landslides. Observing the failure of 73 landslide dams, it was found that 27% of the landslide dams failed within 1 day of formation, and approximately 50% failed within 10 days of formation. They further classified the causes of landslide dam failures into three categories: overtopping, piping, and slope failure, with overtopping being the main cause. Ermini and Casagli (2003) compiled data based on 205 landslide dam cases and found that 40% of the dams failed within a day of formation and 80% failed within a year of formation. Therefore, most landslide dams are short-lived, and the shorter the time the dam takes to fail, the greater the expected damage. Hanson et al. (2005) observed a four-stage breach erosion process for cohesive embankments from seven large-scale overtopping failure tests. The four stages are: (1) the initiation of overtopping and headcut development, (2) the headcut migrating from the downstream to the upstream crest of the embankment, (3) lowering of the crest, and (4) breach widening. During the erosion process of a dam, the overtopping water would downcut the downstream crest of the dam and progress towards the upstream crest of the dam, which would gradually develop into a dam breach, leading to flooding. When the overflow reaches its peak flow, the dimension of the breach then stabilizes slowly. When a landslide dam breaches, a substantial amount of floodwater is released and, because the response time is relatively short, people downstream often have little time to react. Therefore, it is vital to understand the characteristics of floods and erosion caused by the breaching of landslide dams.

Landslides, debris flow, and floods arising from a landslide dam failure will produce acoustic and seismic waves. Under suitable conditions, these acoustic and seismic signals act as an early warning. In this study, the authors measured the acoustic and seismic signals produced by dam breach, floods, and landslides for analysis and further discussed their characteristics, such as frequency content, spectral magnitude, energy variation, and timing of the events. Table 1 contains a summary of the frequency ranges of the seismic signals due to rockfall, debris flow, snow avalanche, or flood events and the sensors used.

To reduce the potential harm caused by flooding events, a method of early detection is required. Huang et al. (2008) used geophones and microphones to measure the seismic and acoustic signals produced by rocks in a riverbed, and their results showed that seismic signals at the soil surface attenuated faster than acoustic signals at high-frequency ranges. Equipment for the detection of acoustic signals may be more valuable in the early detection of natural flooding events than seismic signals as they attenuate less and are therefore able to be detected from a greater distance. Also, Hibert et al. (2011) used seismic signals to analyze the speed, characteristics, and frequency of rockfalls. Their results depicted that the frequency at which free-fall-type rockfalls occurred was centered around 7 Hz, while granular-flow-type rockfall centered at 5 Hz. Furthermore, they proposed a method based on the seismic signals to estimate the volume of rockfalls. Therefore, if sufficient seismic data can be collected, a relationship between seismic signal and landslide volume may be developed.

Debris flow often occurs upstream of the watershed. As a result, if it can be detected early, a warning can be issued to those downstream. Therefore, many studies have been conducted aiming to detect debris flow using different techniques and equipment. Chou et al. (2013) used geophones to measure the

Table 1 Summary of the frequency ranges of seismic signals due to the landslide or flood events from the reviewed literatures

Literature	Sensor	Event	Frequency	Note
Huang et al. (2008)	Geophone, microphone	Rockfall in a river bed	< 50 Hz	Seismic signals attenuated faster than acoustic signals at high frequency
Hibert et al. (2011)	Velocity seismometer	Granular-flow-type rockfall Free-fall-type rockfall	2.7~10 Hz; centered at 5 Hz Centered at 7 Hz	A method was proposed to estimate the volume of rockfall.
Chou et al. (2013)	Geophone	Debris flow	15~30 Hz 25~50 Hz	Frequency is influenced by water content of the debris flow.
Abancó et al. (2014)	Geophone	Debris flow, debris flood, and rockfall	(1) 40~50 Hz (2) 50~60 Hz	(1) Debris flow (2) Debris flood
Kogelnig et al. (2011)	Velocity seismometer, infrasound sensor	Snow avalanche	6 to 8 Hz	Infrasound sensor is suitable for detecting avalanche initiation; combining seismic and infrasound sensors to characterize snow avalanche
Feng (2012)	Velocity seismometer	Flood due to breach of a landslide dam	2.7~2.9 Hz	Spectral magnitude curve helps in estimating the time of dam breach and flooding processes
Yan et al. (2017)	Velocity seismometer	Flood due to breach of two dam models	10~45 Hz	Three frequency bands were identified corresponding to different processes during the dam failure.

seismic signals produced during a gravel-type debris flow at Houyenshan, Miaoli, Taiwan. They concluded that the frequency of the seismic signal induced by the debris flow is influenced by the water content of the debris flow. When the water content is high, the frequency is about 25~50 Hz; when the water content is low, the frequency is about 15~30 Hz. Similarly, Abancó et al. (2014) set up geophones at the Rebaixader catchment of the Spanish Pyrenees and obtained seismic characteristics for debris flows, debris floods, and rock falls. When the surge waves of debris flows were close to the device location, the intensity of the vibration increased rapidly; the frequency range was 40 to 50 Hz. The seismic signals of debris floods were relatively "gentle and smooth" and the intensity was usually lower than that of debris flows; the frequency range was 50 to 60 Hz. Additionally, the seismic signals of rock falls were characterized by high peaks of short duration. From these studies, it can be concluded that different debris material produces different frequencies and peaks, enabling the material to be determined and the flows to be categorized by their frequency and peak height and duration.

There are multiple tools available for the collection of signals from landslide events, including infrared, acoustic, and seismic sensors. Kogelnig et al. (2011) used a combination of seismic and infrasound sensors to estimate the duration of a snow avalanche, yielding highly reliable and accurate results. They also concluded that infrasound sensors are suitable for detecting avalanche initiation. Furthermore, Zhu et al. (2016) used an infrasound sensor to measure the acoustic signals during a rock avalanche and empirical mode decomposition (EMD) to evaluate the characteristics of the low-frequency acoustics caused by the event. They also analyzed the characteristics of the event through time frequency spectrum of the signal. They discovered that it is relatively difficult to identify hazardous events using only infrasonic signals as infrasound sensors are prone to disturbances by weather or wind. This suggests that while infrasound sensors are a powerful tool for the detection of landslide events, their vulnerability to environmental interference often makes them impractical in the field. Similarly, the cost of equipment required to detect infrasound is very high compared with acoustic microphones, reducing the feasibility of their use in early detection systems. Therefore, an approach that utilizes a combination of acoustic and seismic signals at the site could function complementarily while still being economically viable.

Feng (2012) used Hilbert–Huang transform (HHT) to perform a time–frequency analysis of the seismic signal of flooding due to the breach of a landslide dam at Xiaolin Village, Taiwan. The results revealed that spectral magnitude profiles of 2.94 Hz and 2.75 Hz may help in estimating the timing of a landslide dam breach and the subsequent flooding process. The HHT method was also used by Zhu et al. (2017) to analyze the infrasound produced by an earthquake and its subsequent aftershocks. They obtained the intrinsic mode function (IMF) of the signal characteristics as well as main frequency, maximum amplitude, and time–frequency spectrum. The results showed that the use of HHT in the analysis helped to effectively identify hazardous events. This demonstrates that the HHT is a good tool for the determination of frequency content and the spectral magnitude of signals from natural events.

However, natural events are unpredictable, and it is not always possible to record the signals produced by these events. It is therefore important to conduct physical model tests to understand dam-breach flooding events. Yan et al. (2017) reported the result of a double-dam-breach test where they discussed the relationship of the seismic signal to the events of soil collapse, rockslide, and sediment transported by water flow. They identified three frequency bands of the seismic signals that corresponded to three different processes during the dam failure events. This experiment only

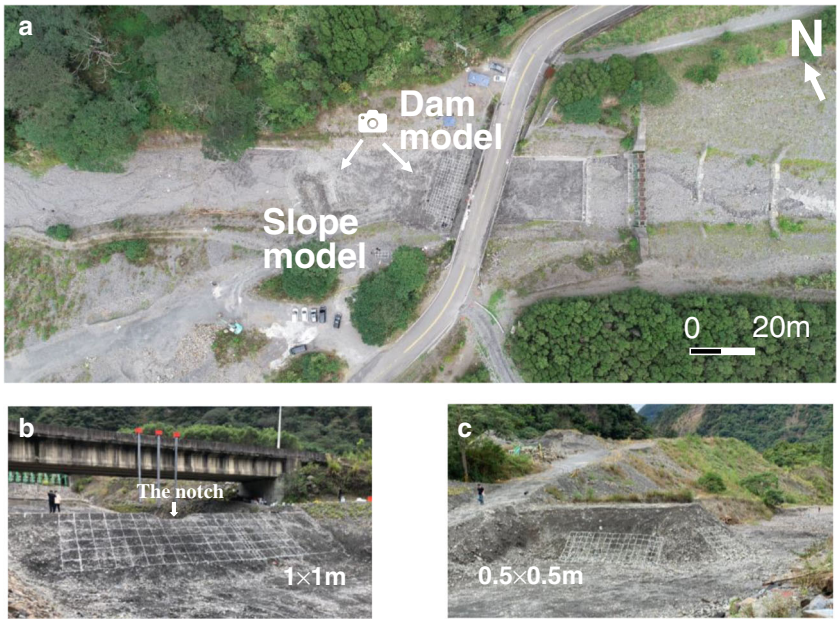

Fig. 1 Photos of the dam and slope models before the test (2018 Nov 01)

relied on one seismic sensor and did not utilize acoustic sensors, limiting the data collected and leaving a clear gap for future experimentation.

Although many of the abovementioned research papers were conducted on the monitoring of landslide events using seismic and acoustic sensors, they focused mainly on landslides, with less regard given to dam-breach flooding. While Feng (2012) has presented the seismic analysis results of an actual dam-breach flooding event, additional seismic data from natural dam breach events is difficult to gather for further study. Similarly, the dam-breach model used by Yan et al. (2017) only examined seismic signals at one location, while an experiment with multiple sensors at multiple locations is needed to gather enough data to determine and examine the change in velocity of flood energy and compare the readings of acoustic and seismic sensors.

Therefore, the present study constructed a physical dam model and a slope model on the streambed of a creek and subjected them to a failure and erosion test, respectively. The study also measured the acoustic and seismic signals produced during the test and analyzed the signals by HHT. The differences in the acoustic and seismic signals produced by the dam model from overtopping to dam failure and the subsequent flood were examined. The spectral magnitudes of both, the acoustic and seismic signals, were compared to identify the sensor that showed earlier signs of dam failure and flood. The velocity of the flood energy was estimated through two approaches. In addition, the landslide volumes of the slope were estimated and their relationship with the Arias intensities of the landslides was established.

Method

Test site and setup

Tests were performed November 1, 2018 on the streambed under the No. 2 Bridge at Huisun Forest Experimental Station (Fig. 1a) in Nantou, Taiwan. The slope of the streambed was approximately 6°. The Neng-Gao Canal water gate which controls when to release water was located upstream of the test site. A dam model was constructed, and an approximately 0.5 m deep notch was kept at the top center of the dam to allow the water to flow through the notch after overtopping and downcutting (Fig. 1b). A slope model was also constructed 40 m downstream from the dam model (Fig. 1c). The dimensions of the dam and slope models are shown in

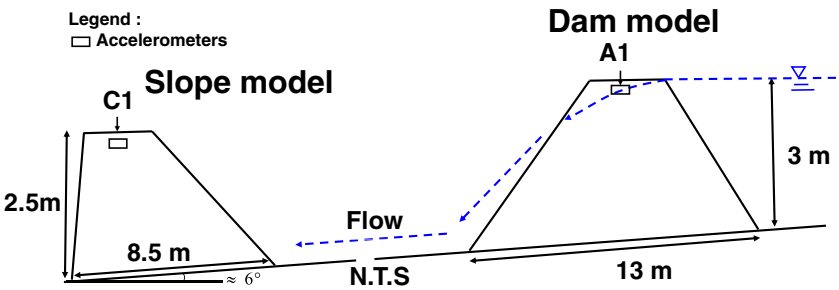

Fig. 2 Cross-sections and approximate dimensions of the dam and slope models

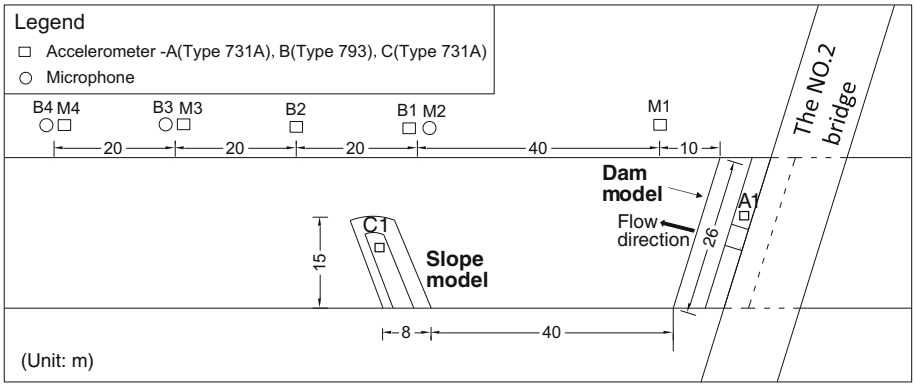

Fig. 3 Layout of the dam and slope models and the sensors

Fig. 2. In the top-view diagram of the test setup (Fig. 3), accelerometers and microphones were installed:

1. Accelerometer A1 (model 731A), located 4 m from the right side of the notch to monitor the seismic signals during the dam failure
2. Microphones M1, M2, M3, and M4, located 10, 50, 90, and 110 m downstream from the dam model to record the acoustic signals produced by the dam failure and flood
3. Accelerometers B1, B2, B3, and B4 (model 793), located on the river bank 50, 70, 90, and 110 m downstream from the dam model to monitor the seismic signals produced by the energy of flood passing the river bank
4. Accelerometer C1 (model 731A), located on the slope model to monitor the seismic signals produced by the flood and landslides on the slope model. This would be caused by floodwater eroding the toe of the slope model

Additionally, a simple method was used to record the changes in water level. Water level markings were drawn on the revetment of the riverbank, and cameras were used to record the water level versus time.

Figure 4 shows the top view of the post-test. The videos of the dam-breach test and the subsequent effect on the slope can be seen in the supplementary material.

Instrumentations

Accelerometers

This study used model 731A and 793 accelerometers produced by Wilcoxon Sensing Technologies to monitor the seismic signals during the test, and their characteristics are shown in Table 2. This study used "economical" types of accelerometers, which are less sensitive to micro-vibrations compared with high-precision broadband seismometers. In practice, the sensors used to monitor landslides are usually like the ones used in this study, affordable, as they are often damaged during landslides. The accelerometers were installed at proximity to energy sources and their safety was considered.

Microphone

This study used the MI-17 microphones produced by ROGA Instruments to record the acoustic signals produced by the flood during the test. The specifications are as shown in Table 3. The microphones were placed on the right bank and designated as M1~M4 (Fig. 3).

Unmanned aerial vehicle

Two DJI Phantom 4 Pro V2.0 unmanned aerial vehicles (UAVs) were flown over the slope model during the test to continuously capture the landslides caused by the erosion of the toe of the slope model. Certain photographs were selected as stereo pairs and processed using Pix4D 4.2.27 software to produce digital elevation models (DEMs), and ArcMap 10.2 was used to estimate sliding

Fig. 4 Top view photo taken a day after the test (2018 Nov 02)

Table 2 Specifications of the accelerometers

Specifications	Wilcoxon 731A	Wilcoxon 793
Sensitivity	10 V/g	100 mV/g
Frequency response	0.1~300 Hz (± 10%)	1.0~7 kHz (± 10%)
Acceleration range	0.5 g peak	80 g peak
Resonance frequency	750 Hz	25 kHz
Height (mm)	53.3	1.78
Diameter (mm)	62.2	1.0

volumes. In volume calculations, the video footage was used to help identify the locations of the landslides. ArcMap was further used to extract the landslide zones and to calculate the volume from the DEMs before and after the landslides. There were six landslide events (S1~S6) that the stereo-paired photos were successfully taken by the UAVs, so they were selected for the relationship analysis of the sliding energy versus sliding volume.

Signal processing method

Hilbert–Huang transform

Hilbert–Huang transform (HHT) was proposed by Huang et al. (1998). HHT is an excellent tool for analyzing unsteady and nonlinear signals and is very suitable for interpreting the acoustic and seismic signals monitored during the test. HHT consists of two parts: the empirical mode decomposition (EMD) and Hilbert transform. After EMD computation, the signals are decomposed into several intrinsic mode functions (IMFs) and one residual component. The Hilbert transform (HT) is performed to obtain the instantaneous frequency and time–frequency spectrum, revealing the relationships between spectral magnitude (i.e., the instantaneous energy), instantaneous frequency, and time. The property of each IMF could also be analyzed to determine the frequency range and energy percentage of each IMF. Some IMFs may be linked to actual physical phenomena, such as flood and landslide events. The Visual Signal 1.5 software (AnCad, Inc. 2013) was utilized for the HHT analysis.

Arias intensity, I_A

Arias intensity, I_A (Arias 1970), is usually used as a measure of the strength of earthquakes and is calculated using Eq. (1). It is a parameter of shaking intensity defined as the time-integral of the square of acceleration:

$$I_A = \frac{\pi}{2g}\int_{t_1}^{t_2}[a(t)]^2 dt \quad (1)$$

where g is gravity and $a(t)$ is acceleration.

Table 3 Specifications of the microphones

Specifications	ROGA MI-17sw
Sensitivity	≈ 50 mV/Pa (1 kHz)
Frequency response	20 Hz~4 kHz (±dB)
Max. peak SPL	≈ 130 dB (ref. 20μPa)
Total length	93 mm

Baseline correction on the seismic signals of the aforementioned six landslide events was performed to eliminate any potential signal offset prior to calculating the Arias intensity.

Results and discussion

Analysis of seismic and acoustic signals

The environmental background signals were monitored for 5 min (0 s~300 s). Water was released at 300 s to slowly accumulate at the upstream side of the dam model. At about T1 = 1356 s (Fig. 5a), the water overflowed, and the overtopping began. Based on the video footage, overtopping water gradually down cut the dam model until the dam burst started at T2 = 1476 s (Fig. 5b) due to the rapid erosion (serious downcutting) leading to flooding. Floodwater then rushed downstream. The authors then defined the timing T2 as the start time of the dam burst.

Figure 6 shows the signal recorded by A1 during the dam failure. At about 1360 s, A1 started to reflect seismic signal due to vibration of the dam and this caused the energy in the time–frequency spectrum (Fig. 6b) to gradually strengthen. The seismic energy reached the maximum at about 1476 s (T2). Although there were many local collapsing and sliding events of the dam materials during the downcutting process, they could not be easily identified from the signal and spectrum because of the severe vibrations/interferences made by the test crews on the dam.

Figure 7 shows the raw acoustic signals recorded by M1, the acoustic decibel curve, and the acoustic time–frequency spectrum during the dam failure. The acoustic signal showed saturation when the signal was relatively intense (Fig. 7a), because the instrument range setting was too small. Moreover, this had no major impact on the results. The acoustic signal was primarily caused by the sound of flowing water and soil movement. As shown in Fig. 7a, when the dam model was overtopped at T1 = 1356 s, M1 (located 10 m from the dam model) recorded acoustic signals. When the dam burst releasing floodwater downstream at T2 = 1476 s, the acoustic decibel increased further (Fig. 7b).

After the frequency and energy percentage of the A1 signals were analyzed and compared with energy trace in the spectrum of Fig. 6, the frequency of 50 Hz, which had relatively high energy, was selected and extracted for the spectral magnitude curve (Fig. 8). Similarly, for the acoustic signal of M1 at the riverbank, the spectral cross-section of the relatively high-energy frequency of 240 Hz was extracted and plotted in the same figure. Figure 8 also depicts the changes in upstream water level. After the dam was severely eroded, the water level of the water stored upstream rapidly subsided (T2 = 1476 s). From the spectral cross-section of A1, the spectral magnitude gradually increased as A1 received seismic signals induced by overtopping that occurred at T1 (1356 s). The spectral magnitude curve (240 Hz) of M1 also gradually increased as M1 received acoustic signals produced by overtopping water.

In Fig. 8, a significant increase in the spectral magnitude (240 Hz) of M1 acoustic signal after T2 was observed owing to the surge water as a result of the dam bursting. In contrast, the surge water did not increase the spectral magnitude (50 Hz) of A1. The spectral magnitude of A1 gradually decreased as the water level decreased. At about T3 = 1524 s, the flood volume was close to its peak value and it corresponded to the maximum spectral magnitude of M1 acoustic signals. Nevertheless, the seismic energy of the dam measured by A1 had begun to stabilize.

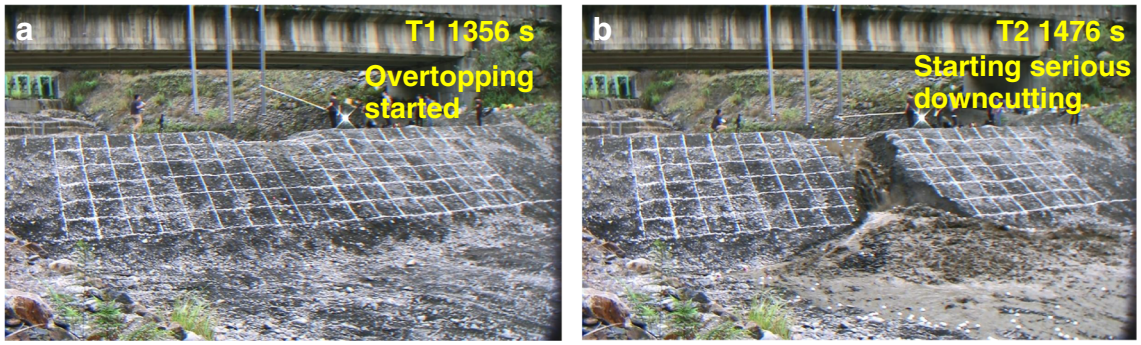

Fig. 5 Pictures of the dam at **a** T1 (1356 s) overtopping started and **b** T2 (1476 s) serious downcutting started

B1 and M2 signals on the riverbank were compared as both sensors were set up at the same location, approximately 50 m from the dam model. Figure 9 shows the seismic signal and time–frequency spectrum of B1 during the dam failure. In Fig. 9b, when the dam model was overtopped at T1 (1356 s), B1 had not yet received seismic signals produced by the flood as the flow volume was low during the initial overtopping. B1 began receiving seismic signals produced by the flood at about 1495 s, and the energy constantly intensified. Figure 10 presents the acoustic signal of M2 during the dam failure event, the acoustic decibel curve, and the acoustic time–frequency spectrum. When the dam model was overtopped at T1 (1356 s), M2 instantly received acoustic signals, despite being located 50 m away from the dam model (Fig. 10b). After T1 (1356 s), the acoustic decibel energy gradually increased.

For the relatively high B1 and M2 seismic energy of 110 Hz and 190 Hz, respectively, the spectral magnitude curves were extracted from Figs. 9b and 10c. The two spectral magnitude curves were plotted together with the flooding water level of the B1 and M2 locations as shown in Fig. 11. The trends of the two curves are similar and both match the increase in water level.

In Fig. 11, M2 began receiving acoustic signals at T_{M2} (1364 s), which was 8 s after overtopping (T1), and the spectral magnitude began to slowly increase. On the other hand, B1 received the seismic signals produced by the flood at T_{B1} (1464 s), which was 108 s after overtopping (T1). In this study, the microphone could receive signals when the water flow with gravel was still relatively small. The accelerometer received seismic signals when the flood-water hit the revetment with a large amount of force or when the water flow energy was strong. Hence, M2 received signals earlier than B1. This indicates that the use of a microphone (acoustic signal) has an advantage over an accelerometer (seismic signal) as it was able to detect dam burst flood signals earlier.

The signals recorded by B4 and M4 located 110 m from the dam model were also both analyzed and are shown in Fig. 12. From the figure, the energy of the flood slowly increases at approximately 1540 s. Figure 13 presents the results of the M4 microphone. As shown in Fig. 13b, M4 began to receive acoustic signals produced by the flood at $T_{M4} = 1480$ s, causing the acoustic decibel to slowly increase (as marked "increasing" in Fig. 13b).

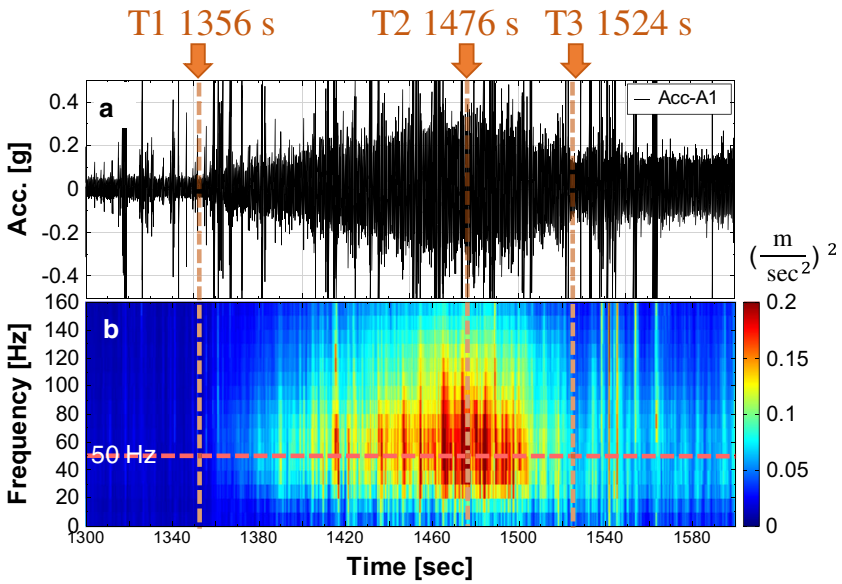

Fig. 6 **a** The seismic signal and **b** the time–frequency spectrum of Accelerometer A1 on the dam model. In the spectrum, the spectral magnitude (instantaneous energy) is plotted with warm color for strong energy (such as red) and cold color for weak energy (such as blue)

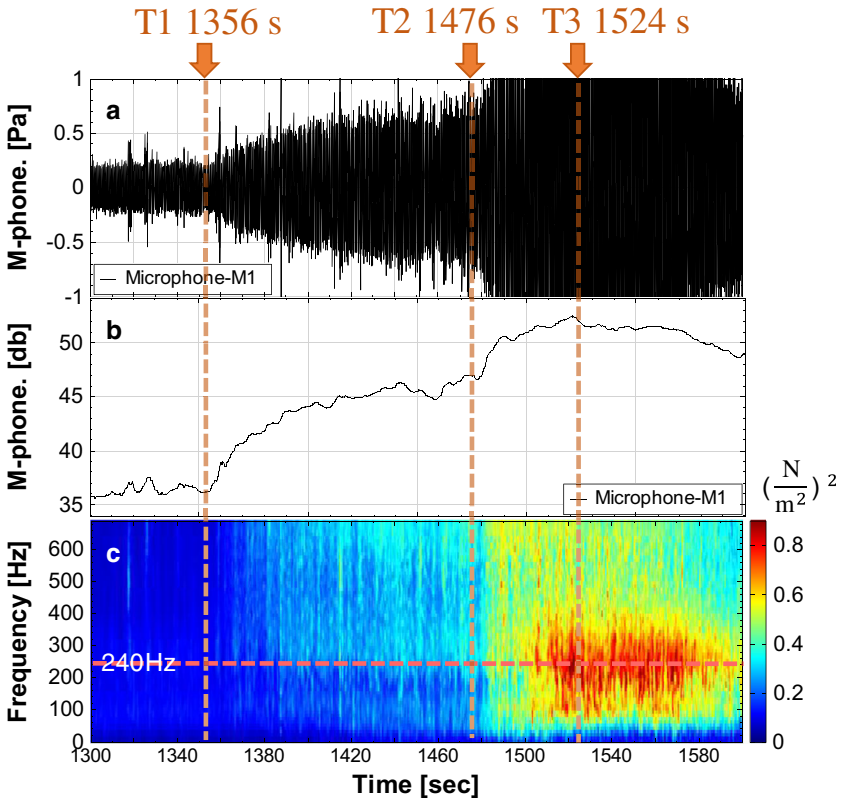

Fig. 7 **a** Acoustic signals. **b** Acoustic decibel curve. **c** Time–frequency spectrum of microphone M1 at the riverbank

Similarly, the spectral magnitude curve of B4 at 130 Hz was plotted with the spectral magnitude curve of M4 at 190 Hz and the water level curve of the location of B4 and M4 in Fig. 14. It was found that the two spectral magnitude curves of the microphone and the accelerometer corresponded well to the increase and decrease in water level. From Fig. 13b, it can be observed that M4 began to receive acoustic signals at T_{M4} (1480 s), but in Fig. 14, the increase in acoustic spectral magnitude of M4 is minimal and not easily identified. The spectral magnitude curve of B4 showed little change in energy produced by the flood until T_{B4} (1520 s), and only then did the spectral magnitude began to increase. Again, by comparing the results of B4 and M4 sensors, it can be concluded

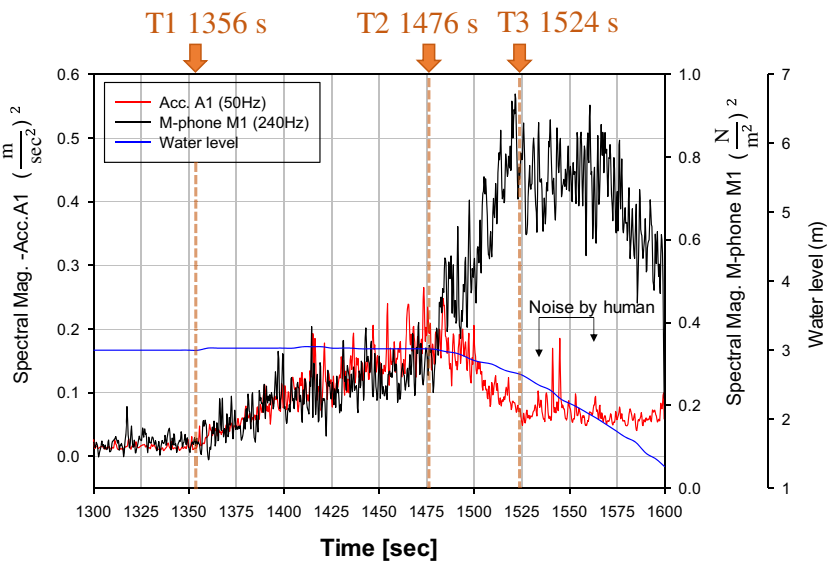

Fig. 8 Spectral magnitude curves of A1 and M1 with water level

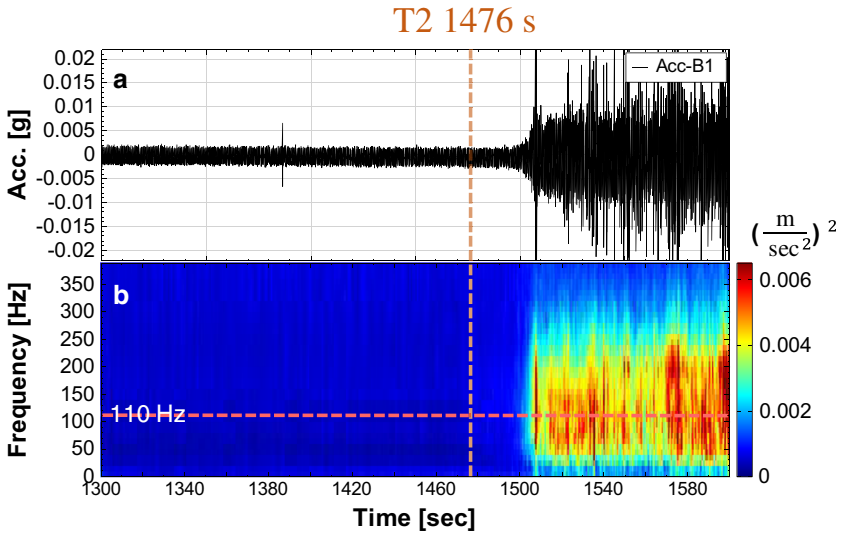

Fig. 9 **a** Seismic signal. **b** Time–frequency spectrum of accelerometer B1 at the riverbank

that the microphone detected signals produced by the dam failure flood earlier than the accelerometer.

Generally, the attenuation of acoustic waves in the air is slower than the attenuation of seismic waves in ground. For example, the echo of sound waves in a valley is transmitted for a long time because the attenuation is slower; in contrast, seismic stress waves attenuate faster. However, as the seismic sensors used in this study were "economical" accelerometers, the range of measurement was somewhat limited; they were only able to detect seismic signals produced by the flood when the water flow from the dam failure was in close proximity or strong enough. High-sensitivity broadband seismometers could

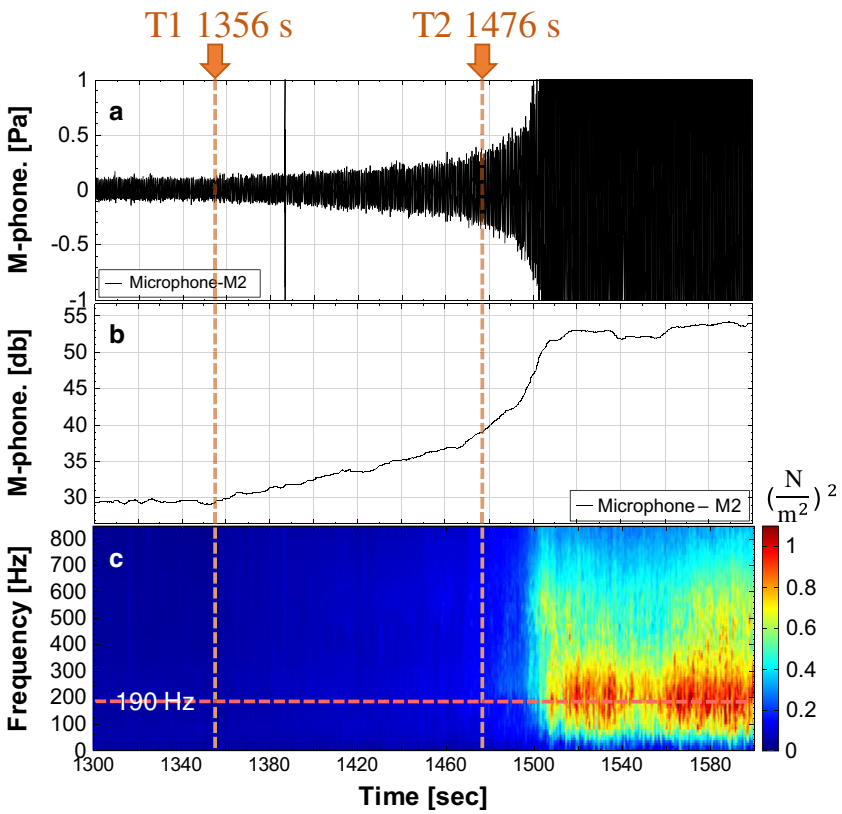

Fig. 10 **a** Acoustic signals. **b** Acoustic decibel curve. **c** Time–frequency spectrum of microphone M2 at the riverbank

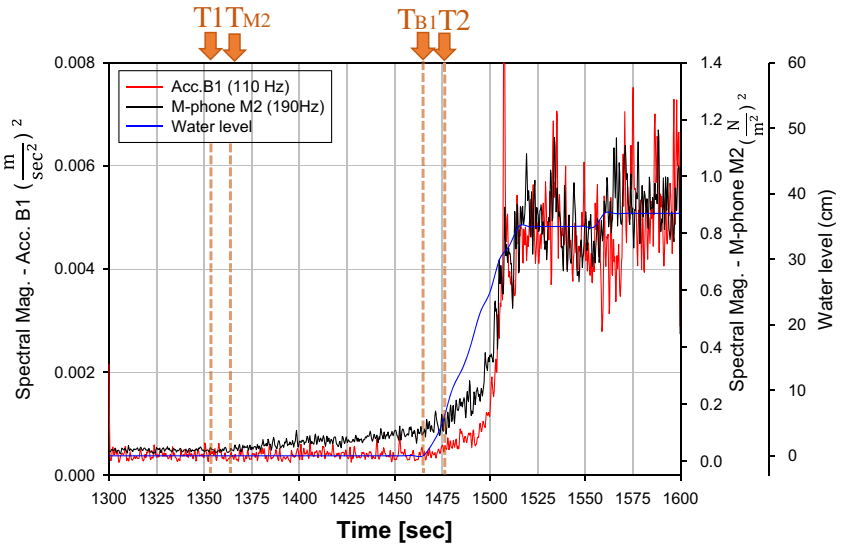

Fig. 11 Spectral magnitude curves of B1 and M2 with water level

perhaps detect seismic signals produced by the flood much earlier.

Estimation of the velocity of the flood energy using riverbank seismic signals

After the acceleration signals of B1–B3 were plotted (Fig. 15), the arrival times of the flood energy at the locations of B1~B3 were estimated. This was done to estimate the velocity of the floodwater flow. The distance between B1 and B3 is 40 m. The traveling time is 7 s. Therefore, the average velocity of the flood energy between B1 and B3 is approximately 5.71 m/s. As shown in Fig. 15, it was obtained from the slope of the red dotted line.

The water levels are plotted as light blue lines in Fig. 15 with the seismic signals of Acc. B1~B4. The relationship between water rise and seismic signals was observed. It can be seen that when the water flow reached the location of the accelerometers, the amplitude of the seismic signals did not increase immediately. This is because when the water flow initially arrived, the energy carried was weak, even when the water level was about 10~20 cm. It was only when the greater energy of the surge wave of the flood arrived at the locations near the accelerometers that the amplitude of the seismic signals started to increase. This proves that the speed estimated in this study is for the velocity of the surge wave of the flood, not for the speed of the first arrival of the water flow.

B4 was slower at receiving seismic signals for several reasons. B4 was located farther from the center of the water flow than other accelerometers, and, because the water passage was wider, the depth of the water flow was shallower, resulting in weaker seismic

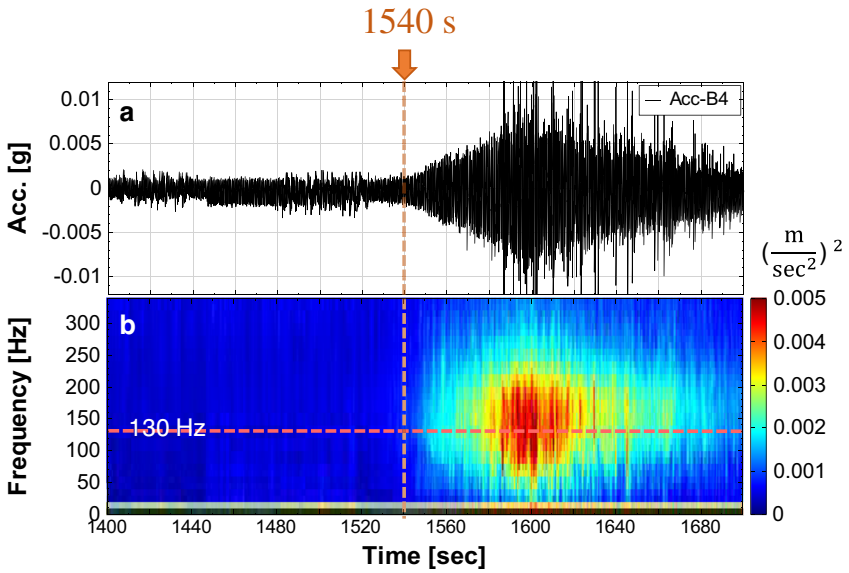

Fig. 12 **a** Seismic signal. **b** Time–frequency spectrum of accelerometer B4 at the riverbank

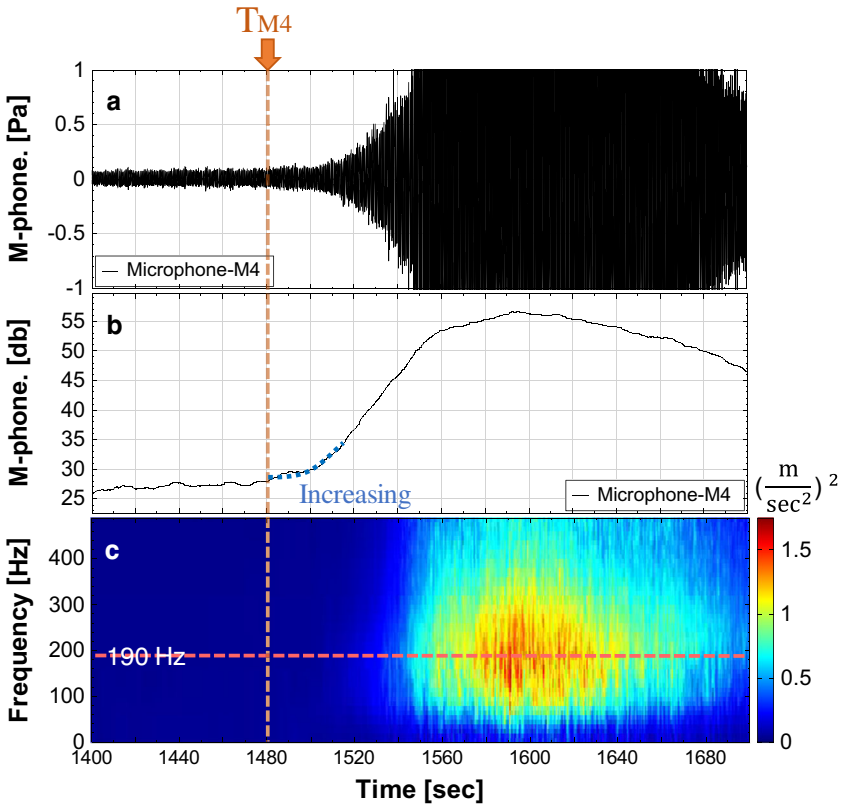

Fig. 13 **a** Acoustic signals. **b** Acoustic decibel curve. **c** Time–frequency spectrum of microphone M4 at the riverbank

signals. The signal attenuation distance was also longer. Therefore, B4 received signals only when the water flow energy was large enough, causing B4 to respond to signals considerably later than the other accelerometers. Therefore, the signals received by B4 were discarded in the calculation of the velocity of the flood.

This study proposed a second method for calculating the velocity of the flood energy, as follows. First, the frequencies with higher seismic energy for B1 to B3 were obtained and their respective spectral magnitude curves were extracted and plotted together in one diagram (Fig. 16). Then, a simple "tangent intersection method" was used to help identify the time points when the spectral magnitude started to increase (as shown by the dotted intersection) in Fig. 16 at which the curvature of each spectral magnitude curve changed considerably. Finally, the time points at which the flood

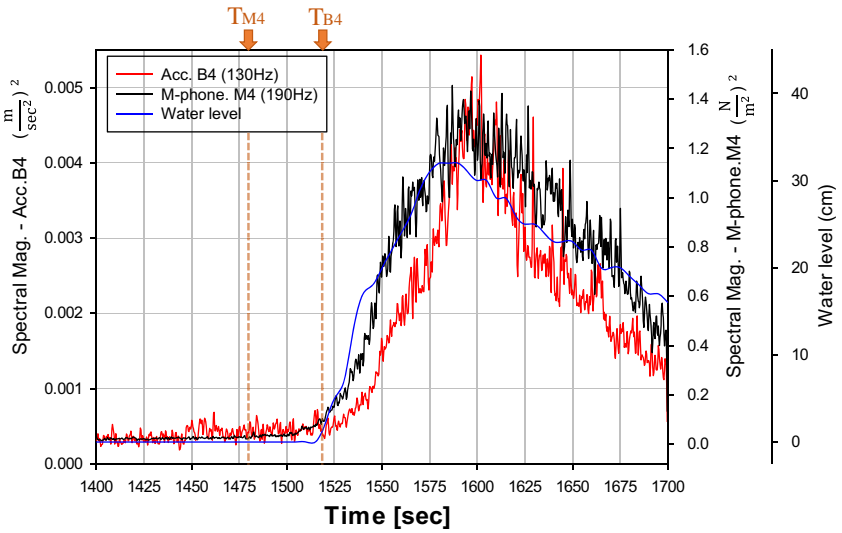

Fig. 14 Spectral magnitude curves of B4 and M4 with water level

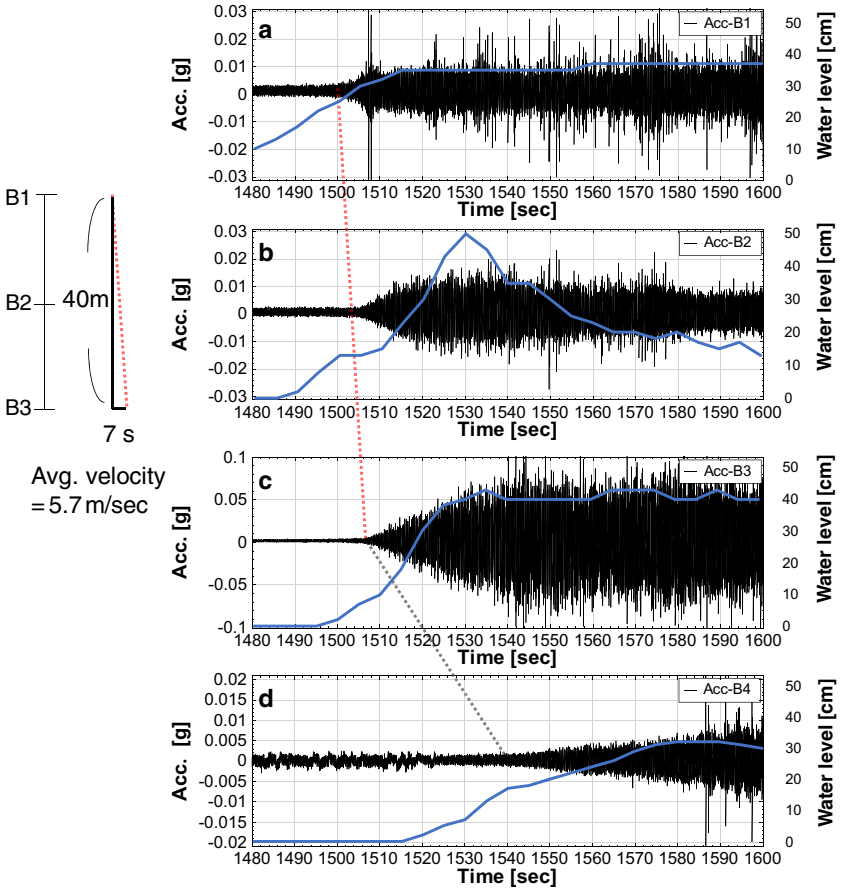

Fig. 15 Seismic signal of accelerometer B1~B4 at the riverbank with water levels

energy reached B1, B2, and B3 were decided on. The velocity of the flood energy in this test was calculated as 5.06 m/s by dividing the distance between the three accelerometers (40 m) by the time difference (7.9 s). The method is new compared to traditional hydrological measurement methods such as the Droppler velocimeter or water level gauge. It is noted that the spectral magnitude curve of B4 is also plotted in Fig. 16 as a reference only.

Analysis of the landslide-related seismic signals of the slope model and the sliding volume

Figure 17 shows (a) the seismic signal, (b) the time–frequency spectrum, and (c) the spectral magnitude curve of the signals monitored by C1 (located on the slope model) for 1400 to 2650 s. The water level at the slope toe is plotted in Fig. 17c. The major vibration frequency of the flood was determined to be

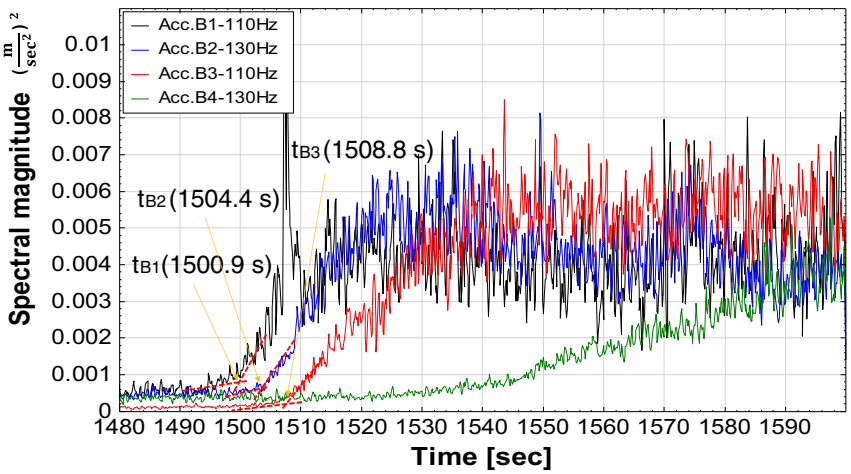

Fig. 16 Spectral magnitude curves of accelerometer B1~B4 at the riverbank

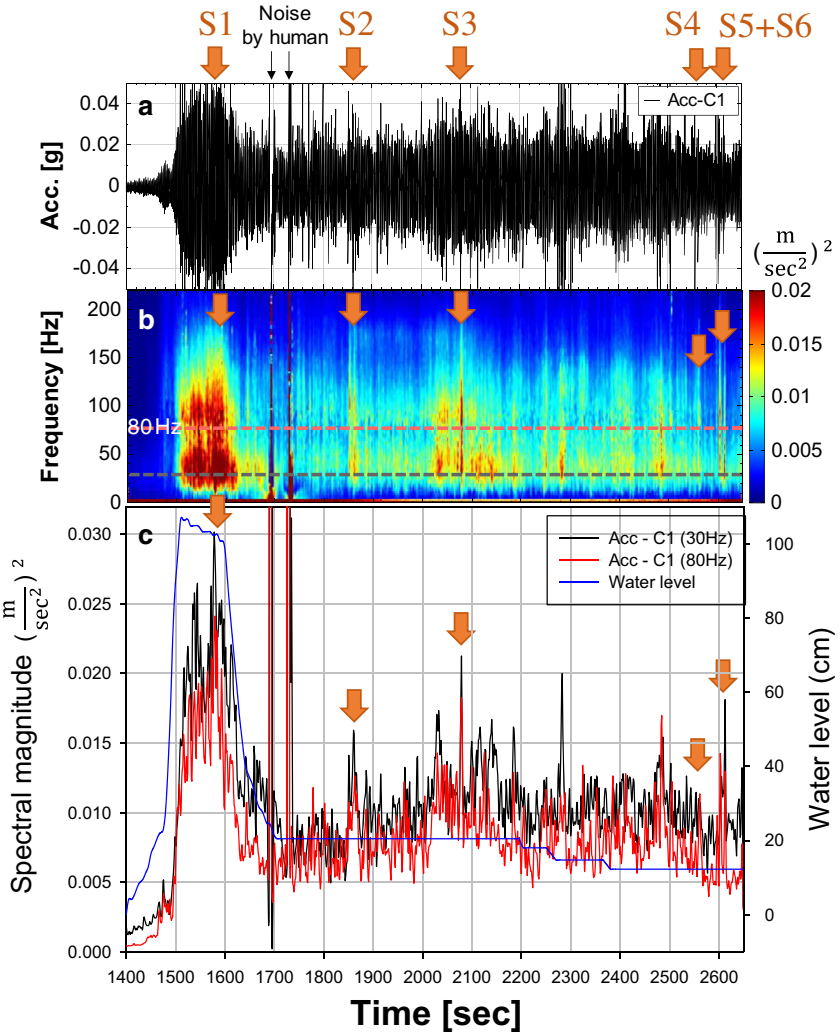

Fig. 17 **a** Seismic signal. **b** Time–frequency spectrum. **c** Spectral magnitude of accelerometer C1 on the slope model

approximately 30 Hz by examining the time–frequency spectrum. The spectral magnitude curve of 30 Hz was extracted to compare with changes in water level.

For the convenience of interpreting the time of collapse, a frequency that was less related to that of the flood was selected for the spectral magnitude curve to highlight the peaks induced by landslides. Therefore, the spectral cross-section of 80 Hz was selected in identifying landslide events. From Fig. 17c, the water level began to rise and severely eroded the toe of the slope model at 1495 s, causing the seismic energy to increase. At about 1600 s, the water level began to drop, and the seismic energy also began to decrease. The spectral magnitude curve of 30 Hz of C1 was well correlated to the flood water level. Generally, when the water level is high and the flow speed is fast, the erodibility of the flood to the slope is also relatively high.

Six landslide events that the UAV had successfully taken stereo photo pairs of were chosen to construct a DEM for landslide volume calculation. These six events corresponded to the peaks in the 80-Hz spectral magnitude curve in Fig. 17c. The pictures of the six landslide areas were outlined with a transparent fluorescent yellow color as shown in Fig. 18. The Arias intensities and landslide volumes were computed as listed in Table 4 and are plotted in Fig. 19. A quadratic relationship between the Arias intensity of the seismic signals of the landslide event and the landslide volume was observed. The S1 landslide event is not included in Fig. 19, because the vibration produced by the flood in the S1 landslide event was relatively much larger; as a result, the Arias intensity was too large and unreasonable.

Comparing the volumes in Table 4 and the spectral magnitudes of the landslide events in Fig. 17c revealed that the landslide volume is directly proportional to the spectral magnitude. From the time frequency spectrum (Fig. 17b) and spectral magnitude curve (Fig. 17c), it is difficult to identify landslide events before 1600 s, because the energy of the flood was large enough that it concealed the signals of the landslides. However, when the flood flow began to recede after 1700 s, it became easier to identify the landslide events.

It is acknowledged that the sliding volumes that occurred on the model slope are relatively small compared to natural landslides. In a future study, should a larger quantity of seismic signal and volume data from natural and larger landslides be available, landslide volume curve versus the Arias intensity has the potential

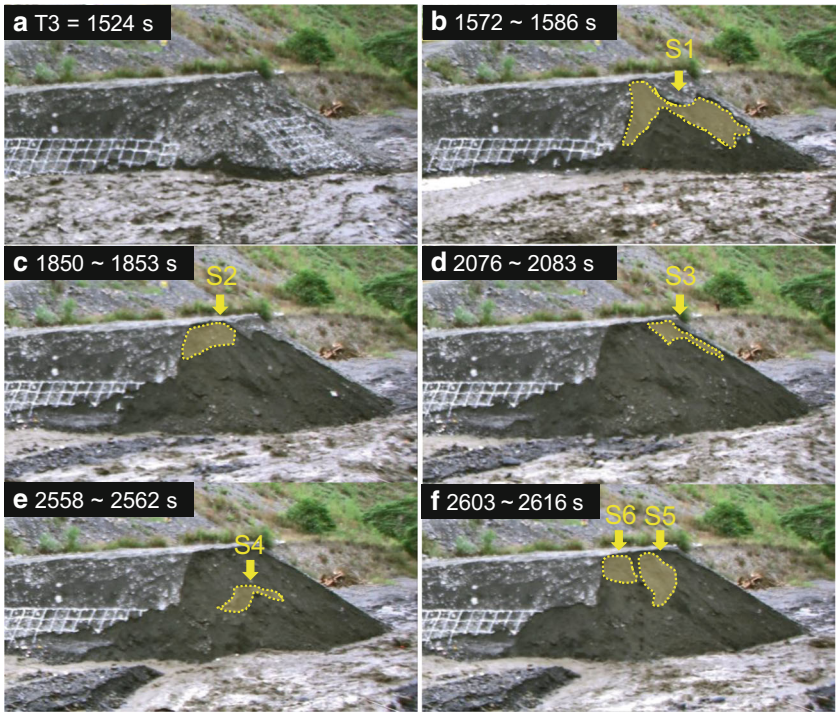

Fig. 18 Pictures of the landslide area of the six events

to be extended to large-scale landslides. As an application, if volume versus Arias intensity relation curve is at hand and if the Arias intensity is calculated from its seismic signal shortly after a landslide, the volume of the landslide can then be promptly estimated based on the relation curve. This will be a useful decision-making tool for disaster mitigation and onsite relief actions.

Conclusions

Based on the findings from the study, the following conclusions were drawn:

1. The seismic signals received by the accelerometers on the dam model were analyzed as time–frequency spectra and spectral magnitude curves. The spectra and spectral magnitude curves corresponded to the process of downcutting erosion of the dam model by the overtopping water. Also, the spectral magnitude curves of the acoustic and seismic signals corresponded well to the water level during the flooding. The flooding level corresponds to the spectral magnitude curve of the seismic signal such that the curve is deemed as a proxy curve of the flooding level.
2. The microphones received signals produced by the overtopping water earlier than the accelerometer, i.e., acoustic signals were received earlier than the seismic signal because acoustic waves are attenuated less than seismic waves. This demonstrates that microphone is quicker than accelerometer in responding to a dam breach and flooding in this study.
3. The arrival time differences of the flood energy were obtained by monitoring the seismic signals at different locations of the riverbank, and then the velocity of flood energy was estimated

Table 4 Arias intensities versus volumes of the six landslide events

Sliding event	Sliding duration (s)	Arias intensity (m/s)	Sliding volume (m^3)
S1	1572~1586	62.13×10^{-5}	2.0795
S2	1850~1853	4.515×10^{-5}	0.6106
S3	2076~2083	12.95×10^{-5}	1.2361
S4	2558~2562	4.179×10^{-5}	0.7262
S5 + S6	2603~2607; 2613~2616	10.04×10^{-5}	0.9853

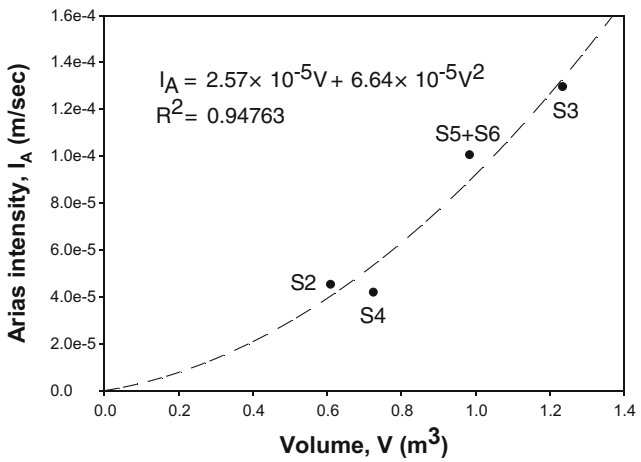

Fig. 19 The relationship between Arias intensity and sliding volumes

as 5.71 m/s. A new method was proposed by using the spectral magnitude curves to estimate the traveling speed of flood energy as 5.06 m/s. In general, the faster the flood velocity, the greater the danger posed to the surrounding areas. If the velocity is obtained in a real flooding event, an emergency warning can be issued with greater confidence.

4. It is difficult to identify landslides occurring during flooding by time-series seismic signals because the signals of landslide and flooding signals overlap. With the help of the time–frequency spectrum and spectral magnitude curve, the identification of landslides during flooding is simplified. Ideally, a landslide corresponds to a peak in a spectral magnitude curve. However, sometimes, it is still difficult to measure a landslide due to the high noise level and lack of energy generated.
5. The six landslide events induced by the toe erosion of the slope during the test were identified from the time–frequency spectrum and test film. The volumes of the six landslides were obtained by using UAVs. A quadratic curve relationship between the landslide volume and Arias intensity was found. This relationship is based on relatively small landslide volumes; therefore, the authors suggest further investigations to verify this relationship for larger and natural landslides.

Acknowledgments

The constructive comments from the reviewers are very appreciated. Acknowledgments are also extended to Dr. Samkele Tfwala and Mr. Hallam Atherton for reviewing the manuscript style, and Mr. Shi-hao Chen and Mr. Lu-jian Zhong for their help in preparing part of the figures.

Funding information

The authors acknowledge the Ministry of Science and Technology, Taiwan, R.O.C, for providing research fund (grant number: 107-2625-M-005-007 and MOST 106-2625-M-005-006-).

References

Abancó C, Hürlimann M, Moya J (2014) Analysis of the ground vibration generated by debris flows and other torrential processes at the Rebaixader monitoring site (Central Pyrenees, Spain). Nat Hazards Earth Syst Sci 14:929–943. https://doi.org/10.5194/nhess-14-929-2014

AnCad Inc (2013) Visual Signal Reference Guide. Version1.5 (in Chinese). http://www.ancad.com.tw/VisualSignal/doc/1.5/RefGuide.html. Accessed 20 May 2019

Arias A (1970) A measure of earthquake intensity. In: Hansen RJ (ed) Seismic design for nuclear power plants. MIT Press, Cambridge, pp 438–483

Chou HT, Lee CF, Huang CH, Chang YL (2013) The monitoring and flow dynamics of gravelly debris flows. J Chin Soil Water Conserv 44(2):144–157 (in Chinese)

Costa JE, Schuster RL (1988) The formation and failure of natural dams. Geol Soc Am Bull 100:1054–1068. https://doi.org/10.1130/0016-7606(1988)100<1054:Tfafon>2.3.Co;2

Ermini L, Casagli N (2003) Prediction of the behavior of landslide dams using a geomorphological dimensionless index. Earth Surf Process Landf 28:31–47. https://doi.org/10.1002/esp.424

Feng ZY (2012) The seismic signatures of the surge wave from the 2009 Xiaolin landslide-dam breach in Taiwan. Hydrol Process 26:1342–1351. https://doi.org/10.1002/hyp.8239

Hanson GJ, Cook KR, Hunt SL (2005) Physical modeling of overtopping erosion and breach formation of cohesive embankments. T ASAE 48(5):1783–1794

Hibert C, Mangeney A, Grandjean G, Shapiro NM (2011) Slope instabilities in Dolomieu crater, Réunion Island: from seismic signals to rockfall characteristics. J Geophys Res-Earth 116:F04032. https://doi.org/10.1029/2011JF002038

Huang NE, Shen Z, Long SR, Wu MLC, Shih HH, Zheng QN, Yen NC, Tung CC, Liu HH (1998) The empirical mode decomposition and the Hilbert spectrum for nonlinear and non-stationary time series analysis. Proc Roy Soc A-Math Phy 454:903–995. https://doi.org/10.1098/rspa.1998.0193

Huang CJ, Yeh CH, Chen CY, Chang ST (2008) Ground vibrations and airborne sounds generated by motion of rock in a river bed. Nat Hazard Earth Sys 8:1139–1147. https://doi.org/10.5194/nhess-8-1139-2008

Kogelnig A, Suriñach E, Vilajosana I, Hübl J, Sovilla B, Hiller M, Dufour F (2011) On the complementariness of infrasound and seismic sensors for monitoring snow avalanches. Nat Hazard Earth Sys 11:2355–2370. https://doi.org/10.5194/nhess-11-2355-2011

Yan Y, Cui P, Chen SC, Chen XQ, Chen HY, Chien YL (2017) Characteristics and interpretation of the seismic signal of a field-scale landslide dam failure experiment. J Mt Sci 14:219–236. https://doi.org/10.1007/s11629-016-4103-3

Zhu X, Xu Q, Zhao ZY, Li TT (2016) Low frequency acoustic signals associated with rock falls, thunderstorms, and wind turbulences in field environment. Appl Acoust 112:131–139. https://doi.org/10.1016/j.apacoust.2016.05.021

Zhu X, Xu Q, Liu H (2017) Using Hilbert–Huang transform (HHT) to extract infrasound generated by the 2013 Lushan earthquake in China. Pure Appl Geophys 174:865–874. https://doi.org/10.1007/s00024-016-1438-1

Electronic supplementary material The online version of this article (https://doi.org/10.1007/s10346-020-01390-x) contains supplementary material, which is available to authorized users.

Z.-Y. Feng · H.-Y. Huang
Department of Soil and Water Conservation,
National Chung Hsing University,
Taichung, Taiwan

Z.-Y. Feng
e-mail: tonyfeng@nchu.edu.tw

H.-Y. Huang
e-mail: a90278a6@gmail.com

S.-C. Chen (✉)
Innovation and Development Centre of Sustainable Agriculture (IDCSA), Department of Soil and Water Conservation,
National Chung Hsing University,
Taichung, Taiwan
Email: scchen@nchu.edu.tw